Research Article Vol. 2, No. 6 / June 2015 / Optica 571

Microelectromechanically reconfigurable interpixelated metamaterial for independent tuning of multiple resonances at terahertz spectral region

Prakash Pitchappa, Chong Pei Ho, Lokesh Dhakar, and Chengkuo Lee*

Department of Electrical and Computer Engineering, National University of Singapore, Singapore 117583, Singapore
**Corresponding author: elelc@nus.edu.sg*

Received 12 March 2015; revised 4 May 2015; accepted 26 May 2015 (Doc. ID 236092); published 18 June 2015

Tunability in metamaterials has added a new dimension to the functionality and application scope for light–matter interaction in the subwavelength regime. Microelectromechanical-systems-based microactuators have been reported as the most straightforward and efficient means of achieving tunable metamaterials, but so far can provide tunability of only a single electromagnetic property. This has greatly limited its usage in applications requiring either simultaneous or independent control of multiple parameters, such as linear polarization switching, actively controlled refractive indices, bandwidth tunable filters, and modulators. Here, we place an electrically isolated split ring resonator and an electrical split ring resonator in an interpixelated fashion to form a metamaterial super cell. The proposed metamaterial can be configured to have only magnetic resonance at 0.59 THz, only electrical resonance at 0.45 THz, or both magnetic and electrical resonances at 0.375 THz. The frequency at which magnetic and electrical resonance occurs is selectively changed by appropriately biasing the signaling lines of respective resonators. The proposed approach can be extended to have as many resonators as desired in a single complex metamolecule. Each of the unit cells is independently addressed and can be programmed, thereby enabling multiple functionalities using a single metamaterial in the terahertz spectral region. We believe that our proposed approach will enable the realization of a wide range of actively controlled EM properties, especially for active control of refractive indices and its potential applications. It will also aid in the realization of the ultimate form of tunable metamaterial, the "THz programmable metamaterial," which will likely be a disruptive technology in the near future.

OCIS codes: (160.3918) Metamaterials; (230.4685) Optical microelectromechanical devices; (160.1245) Artificially engineered materials; (160.2100) Electro-optical materials.

http://dx.doi.org/10.1364/OPTICA.2.000571

1. INTRODUCTION

An electromagnetic (EM) metamaterial is an array of subwavelength structures that are engineered to achieve specific material properties at a desired spectral region. The EM properties of the metamaterials are primarily determined by the unit cell geometry rather than their material composition. This has led to the demonstration of exotic EM properties that usually do not occur in nature, such as artificial magnetism [1], negative refractive index [2], extremely large refractive index [3], subwavelength focusing [4], and wavelength selective perfect absorption [5]. Furthermore, these EM properties can be dynamically altered through external stimuli and are termed as "active metamaterials." Active metamaterials have been reported for the manipulation of varied EM properties such as magnetic resonance [6–8], electrical resonance [9–11], chirality [12,13], absorption [14–17], terahertz (THz) generation [18,19], and near-field coupling in resonators [20–22]. The versatility of these metamaterials has immensely increased the application scope of metamaterials, especially for the THz spectral region, where the response of naturally occurring material is minimal. Some of the widely reported approaches for realizing active THz metamaterials include optically controlled photoconductive materials [10,12,13,16], the electrically controlled refractive index of liquid crystals [8,14,15], the electrically controlled conductivity of doped semiconductor materials [9,11], or graphene [23]. Active metamaterials using the thermally controlled conductivity phase of vanadium oxide [24], magnetically controlled ferrite rods [25], and controlled filling of liquid metals to form the metamaterial unit cell patterns [26] are also reported. However, the use of active material either as a part of metamaterials or as the surrounding medium is not highly scalable owing to the frequency-dependent material properties of naturally occurring active materials. Some of the approaches demand exotic materials that are difficult to process and require bulky setups for providing the control signals, thereby making them not attractive for miniaturized THz systems. Alternatively, microelectromechanical-systems (MEMS)-based structurally reconfigurable metamaterials have been demonstrated as a more straightforward

and efficient way of realizing active metamaterials in the THz spectral region [24–38]. Micromachined actuators of desired dimension, actuation direction, and deformation range are designed and integrated into the metamaterial unit cell. By controlling the physical position of microactuators in the unit cell geometry, the metamaterial response is accordingly tuned. Various types of MEMS actuators have been reported based on the desired functionality to be realized. In-plane movable actuators such as the electrostatic comb drive and 'V'-shaped thermal actuators are used for continuously tunable response with varying anisotropy [27–30]. On the other hand, out-of-plane deformable structures controlled through a thermal, electrostatic, electrothermal, or piezoelectric mechanism are predominantly used for modulation and switching of electrical or magnetic responses with unaltered anisotropy characteristics [31–42]. MEMS actuators are highly miniaturized and electrically controlled and hence can be readily integrated with a metamaterial unit cell without the need for complicated processes or exotic materials.

In the field of active metamaterials, there are primarily two research directions—one is to achieve active control of novel EM properties, and the other is to demonstrate novel control mechanisms to improve the tunable performance of the earlier reported metamaterials. However, in either of the cases the control signal is provided to all the unit cells forming the metamaterial simultaneously, thereby restricting the tunability to a signal EM parameter. This significantly limits the great research potential and application scope possessed by active THz metamaterials. Yet another critical dimension in active metamaterials is the controllability of unit cell states, which specifies how many unit cells forming the metamaterial can be independently controlled, and is relatively unexplored. The routing lines can be isolated to provide independent control at the level of subarray, row, column, or unit cell. If each of the unit cells is controlled independently, then the final states of the metamaterials can be reconfigured by programming the control signals to each unit cell and are termed as "programmable metamaterials" [43–45]. Earlier reports on programmable metamaterials are based on mechanical deformation to achieve tunable flexibility or using diodes for beam steering in the gigahertz spectral range [43,44]. However, these approaches are not scalable to the THz spectral region. Recently, electrothermally actuated MEMS metamaterials for achieving programmable THz metamaterials have been conceptually demonstrated [45]. The ideal scalable technology desired for achieving THz programmable metamaterials is currently unavailable. As a first step towards the realization of programmable metamaterials, two different types of meta-atoms are placed into a single metamolecule, with independent control. In order to retain the symmetry of the metamaterial, the two meta-atoms should be placed diagonally midway between the other unit cells and are termed as "interpixelated metamaterials" [46–48]. A single interpixelated metamaterial can achieve multiple functions, such as tunable anisotropy, tunable bandwidth filters, multispectral imagers, and active polarization control. The most important criterion for the realization of independent control of interpixelated meta-atoms is the localized control of microactuators at the unit cell level. This design requirement limits the choice of control mechanisms that can be used. The conventional method of using active materials controlled through optical, magnetic, or thermal methods can only provide global control. MEMS-based in-plane reconfigurable approaches with comb-drive and V-shaped thermal actuators or out-of-plane deformable thermal bimorph are also not suitable for localized control. Hence, electrostatically actuated out-of-plane deformable cantilevers that are readily integrated into any unit cell geometry with the possibility for isolating electrical routing lines are the best choice for the realization of multifunctional active metamaterials. The varied choice of metamaterial resonators and independent control of these resonators makes the interpixelated MEMS metamaterial highly versatile and potentially disruptive.

In this paper, an interpixelated metamaterial design integrated with MEMS actuators to achieve active control of multiple functionalities, i.e., magnetic and electrical resonances using a single metamaterial, is reported. The proposed metamaterial super cell or metamolecule is formed by placing split ring resonator (SRR) and electrical split ring resonator (eSRR) meta-atoms in an interpixelated fashion, as shown in Figs. 1(a) and 1(b), to enable the excitation of magnetic resonance [49–51] and electrical resonance [52–54], respectively.

2. INTERPIXELATED MEMS METAMATERIAL DESIGN

A. Interpixelated Metamolecule Design

The schematics of the proposed multifunctional interpixelated MEMS metamaterial is shown in Fig. 1(a). Each metamolecule consists of two sets of SRR and eSRR meta-atoms placed diagonally with respect to each other and electrically isolated with each other as shown in Fig. 1(b). The SRR primarily consists of a square ring with a split on one side, and this asymmetry enables the excitation of fundamental inductive–capacitive (LC) resonance that provides the magnetic response, when the incident electric field is along the gap-bearing side of the SRR [46]. Meanwhile, the eSRR is formed by placing two SRRs with overlapped gap-bearing sides as shown in Fig. 1(b). The mirror symmetry in the structure along the gap direction enables the excitation of electrical inductive–capacitive (eLC) resonance, when the incident electric field is along the gap direction [49]. The SRR has a fixed base length (L_{FS}) = 50 μm, side length

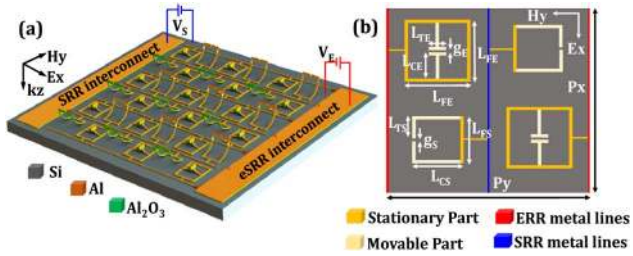

Fig. 1. (a) Schematic of interpixelated MEMS metamaterial. The interpixelated metamaterial consists of SRR and eSRR unit cells with released parts. All the SRR meta-atoms are electrically connected but isolated from the interconnect that connects all the eSRR meta-atoms. The SRRs and eSRRs are independently controlled by selectively applying voltage V_S and V_E, respectively, with respect to the Si substrate. (b) Top view of interpixelated metamolecule and its geometrical parameter definition. Each metamolecule is made of two SRR and two eSRR meta-atoms placed diagonally. The dark-orange part of the meta-atoms refers to the fixed part, while the light-orange part refers to the movable part that is electrostatically actuated. The THz wave with electric field (Ex) along the direction parallel to the gap-bearing side of the SRR and eSRR is normally incident at all times.

(L_{CS}) = 50 μm, gap-bearing tip length (L_{TS}) = 23.5 μm, and in-plane split gap (g_S) = 3 μm as shown in Fig. 1(b). The eSRR unit cell has fixed base length (L_{FE}) = 74 μm, center cantilever length (L_{CE}) = 30 μm, tip length (L_{TE}) = 17 μm, and in-plane split gap (g_E) = 3 μm as shown in Fig. 1(b). The SRR part of the metamolecule will enable the excitation of magnetic resonance, while the eSRR part will provide the electrical resonance for the normally incident THz wave with its electric field along the SRR and eSRR gap-bearing side, i.e., Ex. The resonances in the SRR and e-SRR meta-atoms can be modeled using an equivalent circuit model, with the metallic rings providing the inductive effect, while the split gap and out-of-plane gap between the released part and the Si substrate provide the capacitive effect. So, the LC resonant frequency of a single SRR is given by $\omega_S = (LC)^{-1/2}$ [46]. The eLC resonant frequency of the eSRR is given by $\omega_E = (LC/2)^{-1/2}$ [49]. For active tuning of LC and eLC resonances, metallic ring dimensions can be altered to cause inductive changes, or the in-plane split gap or out-of-plane gap between metal patterns and the Si substrate can be altered to attain capacitance change in the SRR and eSRR meta-atom geometries, respectively. Here, the out-of-plane capacitance formed between the cantilevers incorporated into SRR and eSRR with respect to the Si substrate is varied using an electrostatic mechanism to achieve active tuning of the magnetic and electrical response in the metamaterial, respectively. The release height of the cantilever defines the initial gap between the released cantilevers and the Si substrate and hence its equivalent capacitance. By decreasing the gap, the capacitance will be increased, thereby correspondingly red-shifting the magnetic and electrical resonant frequencies for SRR and eSRR meta-atoms.

The metamaterial was fabricated using a CMOS compatible process as described next. First, an 8" Si wafer is cleaned, and a 100 nm thick thermal SiO_2 layer is deposited using the low-pressure chemical vapor deposition (LPCVD) process. This SiO_2 will act as the sacrificial layer. Photolithography is used to define the anchor regions. With the pattern defined, SiO_2 is dry etched. Now, a 50 nm thick Al_2O_3 layer is deposited using the atomic layer deposition (ALD) process, followed by 500 nm of sputter deposition of Al. It is important to note that now the bimorph (Al/Al_2O_3) layers are in physical contact with Si at the anchor region, and on the other part of the wafer it is on top of SiO_2 layer. Another photolithography step is used to define the cantilevers, frame, metal line, and bond pads. Both Al and Al_2O_3 are dry etched sequentially. Finally, vapor hydrofluoric acid (VHF) is used to isotropically etch away the SiO_2 sacrificial layer, thereby suspending the cantilevers over the Si substrate with an air gap between them. At the anchor region, the bimorphs are in physical contact with Si; hence the VHF release process is not time-controlled, and this ensures for higher yield for the devices. Due to the residual stress in the bimorph cantilevers, the released cantilevers are bent up, thereby increasing the initial tip displacement. The metamolecule is placed in a 2D periodic array with pitch of 240 μm to form the MEMS metamaterial. The optical image (OM) of the fabricated metamaterial and the scanning electron image (SEM) of the metamolecule are shown in Figs. 2(a) and 2(b), respectively. The variation in out-of-plane direction along the length of released cantilevers can be observed in the OM and SEM images shown in Figs. 2(a) and 2(b), respectively. To enable independent control of magnetic and electrical response, the routing metal lines connecting all the SRR meta-atoms are isolated from the metal lines connecting all the eSRR meta-atoms.

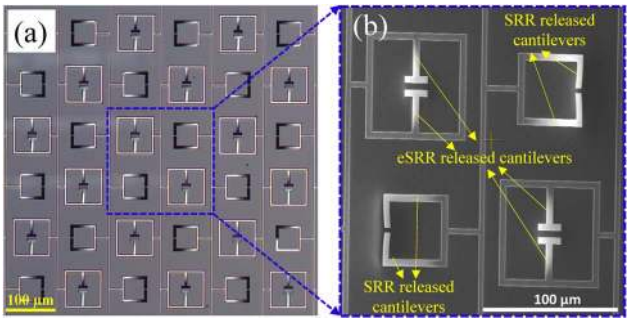

Fig. 2. (a) OM image of the fabricated interpixelated MEMS metamaterial. The gradient of color along the SRR and eSRR unit cells confirms the out-of-plane deformation of the released cantilevers. Owing to the longer release length of SRR cantilevers, the out-of-plane displacement is higher than the eSRR cantilevers as seen qualitatively from the OM image. (b) SEM image of the fabricated metamolecule. The out-of-plane deformation of released cantilevers shows the continuously changing contrast from the fixed part to the tip of released cantilevers.

B. Microactuator Design

In order to achieve active reconfiguration, a certain part of the SRR and eSRR unit cells is released, and their physical position is controlled electrostatically by applying voltage across the released cantilevers and Si substrate. In the SRR meta-atom, the metal routing lines and base arm are permanently fixed to the Si substrate, while the 'L'-shaped structure formed by the side and tip arms is released as shown in Fig. 1(b). In the case of the eSRR meta-atom, the routing lines with outer square ring are fixed to the substrate, and the center 'T'-shaped structures are released. The released cantilevers are bent upwards after the release step as shown in Fig. 2(b). The SRR released cantilever length is approximately 83 μm, while that of the eSRR is 39 μm. The corresponding maximum tip displacement (or initial release height) of the SRR and eSRR cantilevers was measured to be $h_S = 10$ μm and $h_E = 4$ μm, respectively. Based on the length of the released portion and the thickness of the Al and Al_2O_3 layers, the initial release height can be controlled accordingly [42].

When voltage is applied across the released cantilevers and Si substrate, the attractive electrostatic force deforms the suspended cantilevers towards the fixed Si substrate. This mechanical deformation of cantilevers induces a restoring force in the deformed cantilever that opposes the electrostatic force, which caused the deflection in the first place. Hence, the final position of the cantilever at a given voltage is determined by the equilibrium position, where the electrostatic force and restoring force balance each other. As the applied voltage increases, the electrostatic force increases much more rapidly than the restoring force, and at a critical value known as the "pull-in voltage (V_{PI})," the electrostatic force will be higher than the restoring force, thereby bringing the microcantilevers in physical contact with the Si substrate [55,56]. Based on the physical position of the cantilevers, two states are defined as follows: the "OFF" state, when no voltage is applied, and the cantilever is suspended over the Si substrate with air gap, and the "ON" state, defined as the state at which the cantilevers are in physical contact with the Si substrate after

applying voltage higher than V_{PI}. To switch the states of the SRR and eSRR cantilevers, 40 V was applied across the respective cantilevers and Si substrate, which is higher than the V_{PI} of both SRR and eSRR released cantilevers. When the applied voltage is made zero, no electrostatic force exists and the restoring force in the deformed cantilever will bring the cantilever back to its initial "OFF" position. This ensures the repeated operation of the fabricated devices.

3. RESULTS AND DISCUSSION

The electromagnetic responses of the fabricated metamaterials were characterized by measuring the transmission THz spectrum using THz time-domain spectroscopy in transmission mode. The experimental measurements were performed at room temperature in a nitrogen-filled chamber. All the measured transmission spectra are normalized with the transmission spectrum through bare Si thickness of the same thickness as the metamaterial Si substrate. The incoming THz pulse was incident normally with the electric field along the gap-bearing side of the SRR and eSRR meta-atoms. To experimentally verify the tunability of the proposed metamaterial, electrostatic actuation was realized by applying two direct current (DC) voltages—V_S across the SRR interconnect and Si substrate and the other voltage V_E across the eSRR interconnect and Si substrate. The SRR and eSRR bimorph cantilevers can be in "OFF" or "ON" state independent of each other. The interpixelated MEMS metamaterial can therefore be in one of four possible states: S-OFF/E-OFF, S-OFF/E-ON, S-ON/E-OFF, and S-ON/E-ON, as schematically shown in Figs. 3(a), 3(b), 3(c), and 3(d), respectively. In order to elucidate the resonance mechanism, finite-difference time-domain (FDTD) numerical simulations were conducted using CST software. The incoming THz waves were incident normally with electric field along the gap-bearing side of the SRR and eSRR meta-atoms in specific metamaterial configurations. In the simulation, a single super cell was modeled with unit cell boundary conditions employed in axial directions orthogonal to the incident waves. For the structural layers, Si and Al_2O_3 layers were modeled as lossless dielectric with refractive index of 3.416 and 3.1, respectively, and Al was modeled as metal with conductivity of 2e7 $S \cdot m^{-1}$.

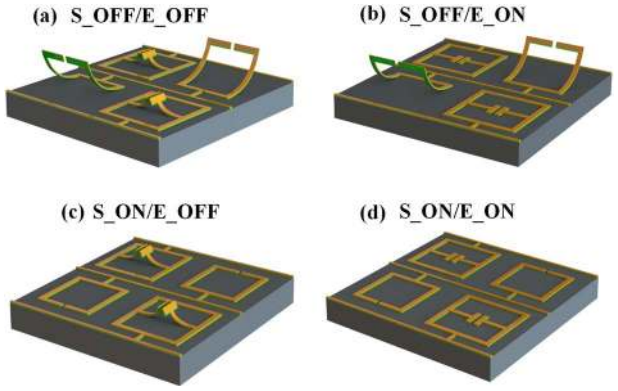

Fig. 3. Schematics of four possible configuration states for the interpixelated MEMS metamaterial: (a) S_OFF/E_OFF; (b) S_OFF/E_ON; (c) S_ON/E_OFF; and (d) S_ON/E_ON.

A. Excitation of Magnetic and Electrical Resonances

The fabricated interpixelated MEMS metamaterial after the release process is in S-OFF/E-OFF state, and the OM image is shown in the inset of Fig. 4(a). Due to the out-of-plane deformation, the tips of the SRR and eSRR cantilevers in the inset are out of focus with respect to the fixed parts of the metamolecule, which are clearly in focus. The transmission spectra of the metamaterial in S-OFF/E-OFF state were measured and are shown with a red-dot line in Fig. 4(a). There are two distinct resonances at 0.45 and 0.59 THz. The simulated transmission spectrum for the S-OFF/E-OFF configuration is shown as a black-solid line in Fig. 4(a). The simulated transmission spectrum matches quite well with the measured one.

The small mismatch between the simulated and measured spectra can be attributed to the variation in the geometrical parameters and the deviation of the material properties used in simulation from the real case. The surface current distributions at the resonances were simulated to determine the resonance modes. Figure 4(b) shows the simulated surface current at 0.45 THz, and the out-of-phase circulating currents induced in the two rings of the eSRR meta-atom, and there is no obvious current in the SRR meta-atoms. Hence, the resonance mode at 0.45 THz should be the electrical LC resonance [49]. Meanwhile, at 0.59 THz, the circulating current is observed in the SRR meta-atoms and the eSRR meta-atoms are relatively passive as shown in Fig. 4(c). Hence, the resonance mode at 0.59 THz should be the fundamental LC mode resonance supporting the magnetic

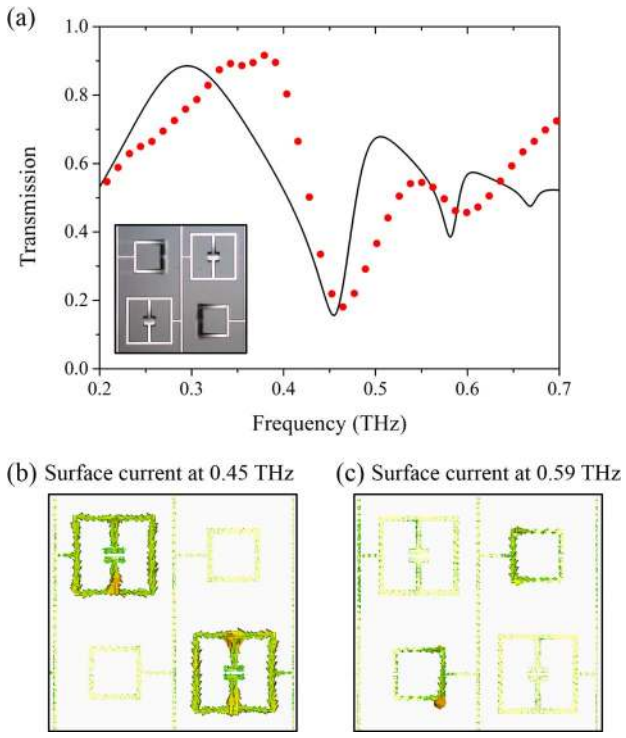

Fig. 4. (a) The simulated (black-solid) and measured (red-dot) transmission spectra for the interpixelated MEMS metamaterial in S-OFF/E-OFF configuration. The inset shows the OM image of the fabricated metamaterial in the corresponding S-OFF/E-OFF configuration. (b) Simulated surface current at 0.45 THz shows the excitation in the eSRR meta-atom, thereby confirming the electrical LC resonance. (c) Simulated surface current at 0.59 THz is excited majorly in the SRR meta-atom, thereby suggesting magnetic LC resonance.

response in the metamaterial [46]. Hence, the metamaterial in S-OFF/E-OFF configuration provides electrical resonance at 0.45 THz and magnetic resonance at 0.59 THz supported by eSRR and SRR meta-atoms in their OFF states, respectively.

B. Switching of Magnetic Resonance

In order to actively control the frequency at which magnetic resonance occurs, the release height of SRR cantilevers (h_S) is selectively switched by applying voltage across SRR interconnects and the Si substrate ($V_S = 40$ V). Meanwhile, the eSRR interconnects and Si substrate are kept in zero potential as the Si substrate ($V_E = 0$ V). The metamaterial is now switched to the S-ON/E-OFF configuration as shown in the inset of Fig. 5(a). The simulated (black-solid line) and measured (red-dot line) transmission spectra for the metamaterial in the S-ON/E-OFF configuration are shown in Fig. 5(a).

After the SRR cantilevers are snapped down to the Si substrate, two resonances occur at 0.35 and 0.45 THz. The simulated surface current at 0.35 THz shows a strong circulating current excited in the SRR meta-atoms as seen from Fig. 5(b). This ensures that the magnetic resonance is switched from 0.59 THz in the SRR OFF state to 0.35 THz in the SRR ON state. Meanwhile, the antiparallel current configuration is retained in the eSRR meta-atoms at 0.45 THz and so remains unchanged with respect to switching of SRR cantilevers as shown in Fig. 5(c). The magnetic resonant frequency switching range of 0.24 THz is measured, corresponding to a change of 10 μm in the release height of the SRR cantilevers. Hence by controlling the released height of SRR cantilevers, the OFF-state magnetic resonance and hence the switching range can be readily designed. It is also important to note that the resonance strength is much higher in the ON state for the SRR compared to the OFF state, which can be quantitatively observed from the current density induced in the SRR rings in OFF and ON states as shown in Figs. 4(c) and 5(b), respectively.

C. Switching of Electrical Resonance

The electrical resonance is excited in the eSRR part of the meta-molecule and so can be actively switched by controlling the release height of the eSRR cantilevers. By selectively applying a voltage, $V_E = 40$ V, across the eSRR interconnect and Si substrate, the eSRR cantilevers were snapped down to the Si substrate. Meanwhile, the SRR cantilevers are kept at the same zero potential ($V_S = 0$ V) as the Si substrate, and so the SRR cantilevers remain suspended with an air gap between the SRR cantilevers and the Si substrate. The current configuration of the metamaterial in S-OFF/E-ON is shown in the inset of Fig. 6(a). The simulated (black-solid line) and measured (red-dot line) transmission spectra of the interpixelated MEMS metamaterial in the S-OFF/E-ON configuration are shown in Fig. 6(a). As the eSRR cantilevers were snapped to the Si substrate, the electrical

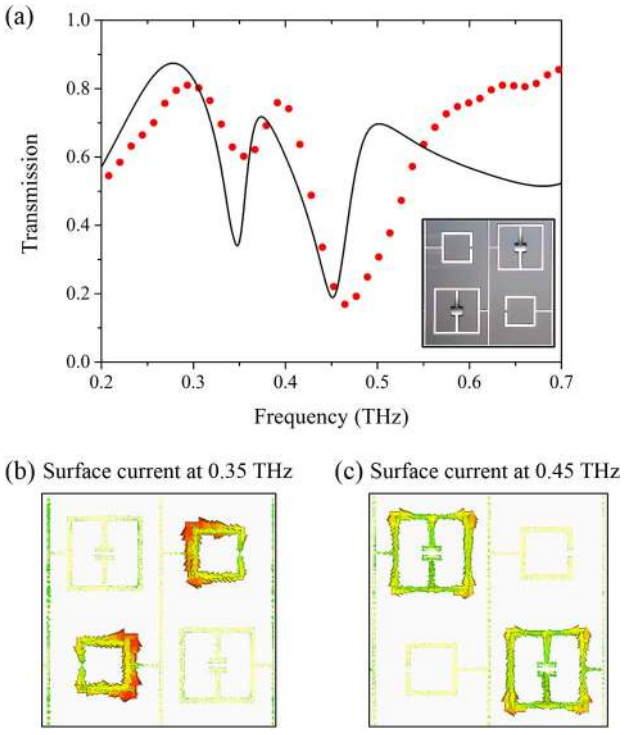

Fig. 5. (a) Simulated (black-solid) and measured (red-dot) transmission spectra for the interpixelated MEMS metamaterial in S-ON/E-OFF configuration. The inset shows the OM image of the fabricated device in the corresponding S-ON/E-OFF configuration. (b) Simulated surface current at 0.35 THz shows the excitation in SRR meta-atom, hence confirming the switching of magnetic resonance to 0.35 THz. (c) Simulated surface current at 0.45 THz is in eSRR meta-atom, and hence confirms that the electrical resonance is unaffected with SRR switching.

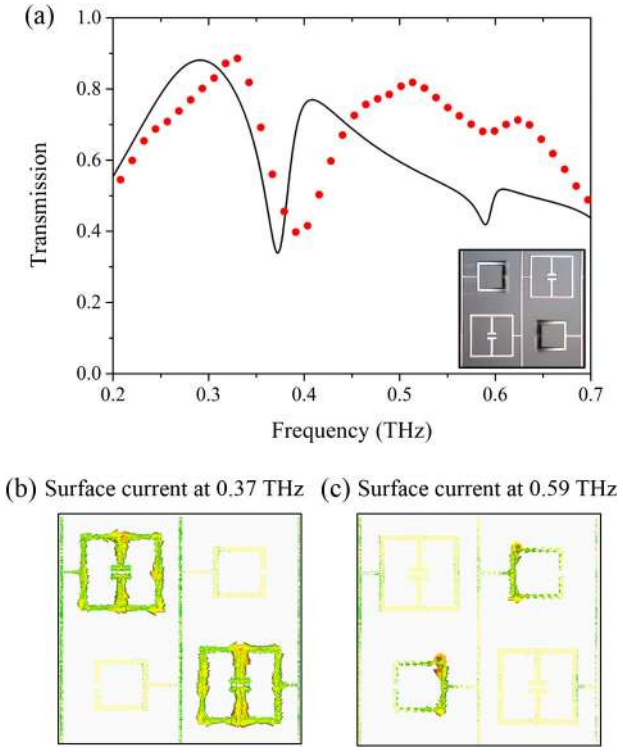

Fig. 6. (a) Simulated (black-solid) and measured (red-dot) transmission spectra for the interpixelated MEMS metamaterial in S-OFF/E-ON configuration. The inset shows the OM image of the fabricated device in the corresponding S-OFF/E-ON configuration. (b) Simulated surface current at 0.37 THz shows the excitation in eSRR meta-atom, hence confirming the switching of electrical LC resonance to 0.37 THz. (c) Simulated surface current at 0.59 THz is in SRR meta-atom, and hence confirms that the magnetic resonance is unaffected with switching of eSRR cantilevers.

resonance frequency switched from 0.45 THz in the E-OFF state to 0.4 THz for the current E-ON state and is confirmed by the antiparallel current configuration in the eSRR meta-atoms as shown in Fig. 6(b). However, the magnetic resonance excited in the SRR meta-atoms remains unchanged at the OFF-state frequency of 0.59 THz, as confirmed by the simulated circulating current configuration as shown in Fig. 6(c). Thus, the electrical resonance is also switched independently from 0.45 and 0.4 THz, without affecting the magnetic response at 0.59 THz. The switching frequency of electrical resonance is 0.05 THz for the out-of-plane deformation of 4 μm for eSRR released cantilevers.

D. Simultaneous Switching of Magnetic and Electrical Resonances

The enhanced controllability of the interpixelated MEMS metamaterial also enables the simultaneous switching of both magnetic and electrical resonances of metamaterial. The SRR and eSRR interconnects are both applied with a voltage of 40 V with respect to the Si substrate. The SRR and eSRR released cantilevers are snapped down, and the metamaterial is reconfigured to the S-ON/E-ON state. The simulated (black-solid line) and measured (red-dot line) transmission spectra of the metamaterial in S-ON/E-ON are shown in Fig. 7(a). Figure 7(b) shows the OM image of the fabricated interpixelated MEMS metamaterial in the S-ON/E-ON state.

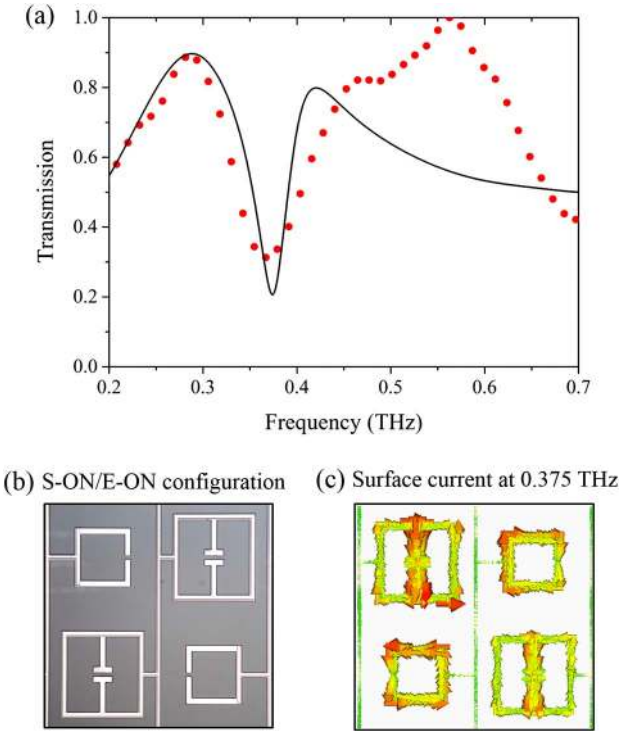

Fig. 7. (a) Simulated (black-solid) and measured (red-dot) transmission spectra for the interpixelated MEMS metamaterial in S-ON/E-ON configuration. (b) OM image of the fabricated metamolecule in S-ON/E-ON configuration. All the features of SRR and eSRR meta-atoms are in focus and thus show that they are snapped down to the Si substrate. (c) Simulated surface current for S-ON/E-ON configuration at 0.375 THz. Both the SRR and eSRR meta-atoms are excited and hence cause the magnetic and electrical resonance to coincide at the same frequency.

It can be seen that the entire metamolecule is in focus, thus confirming the physical snap down of both SRR and eSRR released cantilevers in their respective ON states. The transmission spectrum shows a single resonance at 0.375 THz. The simulated current distribution indicates the excitation of both magnetic and electrical resonance in SRR and eSRR meta-atoms. The ON-state resonant frequency of the uninterfered SRR (eSRR) meta-atoms was measured to be 0.35 THz (0.4 THz). When both the meta-atoms are switched to the ON state, the two closely spaced SRR and eSRR ON-state resonances merge together to provide a single superimposed resonance at 0.375 THz. Hence, in the S-ON/E-ON configuration the metamaterial has a single band response with the excitation of both magnetic and electric resonance at that specific frequency.

As a design principle, the SRR and eSRR unit cell geometries are determined based on the desired ON-state resonant frequency [39]. When scaling up the unit cell dimension both the ON-state magnetic and electrical resonance frequencies can be designed for lower values. With the in-plane dimension of metamaterial unit cells fixed, the OFF-state resonant frequency can be designed based on the capacitance between the released cantilevers and the Si substrate; by controlling the length of unit cell released, the release height, and hence the desired OFF-state resonant frequency can be achieved [42]. The simple microcantilever-based metamaterials are highly versatile and scalable, and therefore can be readily redesigned to operate in far-, mid-, or near-IR spectral regions.

4. PROSPECTIVE OF INTERPIXELATED MEMS METAMATERIALS

The interpixelated MEMS metamaterial opens up a whole new dimension for the controllability and functionalities for active metamaterials. With the proposed independently controlled interpixelated SRR and eSRR metamaterials, various electro-optic functionalities can be achieved, such as simultaneous tuning of multiband resonances, switching of magnetic and electrical resonances at a given frequency, and dynamic control of spectral bands. Additionally, the control of magnetic and electrical resonance enables the manipulation of magnetic permeability and electrical permittivity, respectively, and can have disruptive applications in the future. Interpixelating independently controlled unit cells will form the technological platform for the realization of numerous interesting applications. For instance, linear polarization switching can be simply achieved by interpixelating two identical unit cells of SRRs that are rotated by 90° with respect to each other. Thus one of the unit cells will be responsive to the TE mode, while the other rotated by 90° will be responsive for the TM mode at the same frequency owing to the identical geometries of both unit cells. Furthermore, the MEMS actuators can dynamically control the polarization response across different frequencies. Another attractive application that can be readily realized is the tunable multicolor absorbers by adding in a continuous metallic reflector and a dielectric layer with appropriate thickness between the reflector and interpixelated metamaterial layers [17]. These metamaterials can achieve tunable bandwidth devices, where one of the interpixelated unit cells is fixed at all times and the other is actively controlled to shift the resonance by a desired value to achieve broadband characteristics.

The interpixelation of the metamaterial unit cell with isolated MEMS control is an efficient method and is highly scalable to the

entire region of EM spectrum. Additionally, all the materials and processes are completely CMOS compatible and so can be readily used for batch manufacturing. In the future, more number of unit cells can be interpixelated into a single super cell and can enable more sophisticated features to be realized using a single metamaterial. More interestingly, the progressive enhancement in controllability will ultimately result in micromachined programmable metamaterials, where each of the unit cells can be controlled independently. By coding the state of each unit cell, a single programmable metamaterial can be transformed to operate as a tunable filter, multicolor modulator, broadband electro-optic switch, gradient metamaterial, or even a random metamaterial. Thus, it has immense potential to be the next disruptive technology in the field of actively controlled engineered materials.

5. CONCLUSION

Programmable metamaterials with the ability to function as a tunable filter, spatial light modulator, or gradient metamaterial by programming the biasing conditions of individual unit cells will be the next disruptive technology in the field of THz metamaterials. From the existing single functionality tunable metamaterial, we have demonstrated interpixelated MEMS metamaterials as the access route for the realization of THz programmable metamaterials. The interpixelated MEMS metamaterial that is made of electrically isolated SRR and eSRR meta-atoms placed diagonally to each other for active switching of magnetic and electrical resonances has been experimentally demonstrated. The proposed interpixelated MEMS metamaterial provides switchable dual band characteristics, where the electrical resonance can be switched from 0.45 to 0.4 THz, while the magnetic resonance can be switched from 0.59 to 0.35 THz. When both the SRR and eSRR are switched to the ON state, the metamaterial shows single band characteristics with excitation of both magnetic and electrical resonances at 0.375 THz. The enhanced controllability enables independent and simultaneous control of electrical and magnetic resonances. The reported concept of interpixelating various types of unit cells can be scaled up to have more meta-atoms with unique functionalities to be part of a more complex metamolecule, so as to achieve an independently controlled multifunctional metamaterial. The interpixelated metamaterial paves the way towards the realization of programmable metamaterials with higher intelligence, i.e., individual unit cell control with programmable controls.

Ministry of Education - Singapore (MOE) (ARF-Tier 2, MOE2012-T2-2-154).

REFERENCES

1. T. J. Yen, W. J. Padilla, N. Fang, D. C. Vier, D. R. Smith, J. B. Pendry, D. N. Basov, and X. Zhang, "Terahertz magnetic response from artificial materials," Science **303**, 1494–1496 (2004).
2. D. R. Smith, W. J. Padilla, D. C. Vier, S. C. Nemat-Nasser, and S. Schultz, "Composite medium with simultaneously negative permeability and permittivity," Phys. Rev. Lett. **84**, 4184–4187 (2000).
3. M. Choi, S. H. Lee, Y. Kim, S. B. Kang, J. Shin, M. H. Kwak, K.-Y. Kang, Y.-H. Lee, N. Park, and B. Min, "A terahertz metamaterial with unnaturally high refractive index," Nature **470**, 369–373 (2011).
4. N. Fang, H. Lee, C. Sun, and X. Zhang, "Sub–diffraction-limited optical imaging with a silver superlens," Science **308**, 534–537 (2005).
5. N. I. Landy, S. Sajuyigbe, J. J. Mock, D. R. Smith, and W. J. Padilla, "Perfect metamaterial absorber," Phys. Rev. Lett. **100**, 207402 (2008).
6. J. Han, A. Lakhtakia, and C. W. Qiu, "Terahertz metamaterials with semiconductor split-ring resonators for magnetostatic tunability," Opt. Express **16**, 14390–14396 (2008).
7. T. Driscoll, H. T. Kim, B. G. Chae, B. J. Kim, Y. W. Lee, N. M. Jokerst, S. Palit, D. R. Smith, M. Di Ventra, and D. N. Basov, "Memory metamaterials," Science **325**, 1518–1521 (2009).
8. Z. Liu, C. Y. Huang, H. Liu, X. Zhang, and C. Lee, "Resonance enhancement of terahertz metamaterials by liquid crystals/indium tin oxide interfaces," Opt. Express **21**, 6519–6525 (2013).
9. H. T. Chen, W. J. Padilla, J. M. O. Zide, A. C. Gossard, A. J. Taylor, and R. D. Averitt, "Active terahertz metamaterial devices," Nature **444**, 597–600 (2006).
10. H. T. Chen, J. F. O'Hara, A. K. Azad, A. J. Taylor, R. D. Averitt, D. B. Shrekenhamer, and W. J. Padilla, "Experimental demonstration of frequency-agile terahertz metamaterials," Nat. Photonics **2**, 295–298 (2008).
11. W. L. Chan, H. T. Chen, A. J. Taylor, I. Brener, M. J. Cich, and D. M. Mittleman, "A spatial light modulator for terahertz beams," Appl. Phys. Lett. **94**, 213511 (2009).
12. G. Kenanakis, R. Zhao, N. Katsarakis, M. Kafesaki, C. M. Soukoulis, and E. N. Economou, "Optically controllable THz chiral metamaterials," Opt. Express **22**, 12149–12159 (2014).
13. S. Zhang, J. Zhou, Y. S. Park, J. Rho, R. Singh, S. Nam, A. K. Azad, H. T. Chen, X. Yin, A. J. Taylor, and X. Zhang, "Photoinduced handedness switching in terahertz chiral metamolecules," Nat. Commun. **3**, 942 (2012).
14. D. Shrekenhamer, W. C. Chen, and W. J. Padilla, "Liquid crystal tunable metamaterial absorber," Phys. Rev. Lett. **110**, 177403 (2013).
15. S. Savo, D. Shrekenhamer, and W. J. Padilla, "Liquid crystal metamaterial absorber spatial light modulator for THz applications," Adv. Opt. Mater. **2**, 275–279 (2014).
16. H. R. Seren, G. R. Keiser, L. Cao, J. Zhang, A. C. Strikwerda, K. Fan, G. D. Metcalfe, M. Wraback, X. Zhang, and R. D. Averitt, "Optically modulated multiband terahertz perfect absorber," Adv. Opt. Mater. **2**, 1221–1226 (2014).
17. F. Hu, Y. Qian, Z. Li, J. Niu, K. Nie, X. Xiong, W. Zhang, and Z. Peng, "Design of a tunable terahertz narrowband metamaterial absorber based on an electrostatically actuated MEMS cantilever and split ring resonator array," J. Opt. **15**, 055101 (2013).
18. I. Chatzakis, P. Tassin, L. Luo, N. H. Shen, L. Zhang, J. Wang, T. Koschny, and C. M. Soukoulis, "One- and two-dimensional photoimprinted diffraction gratings for manipulating terahertz waves," Appl. Phys. Lett. **103**, 043101 (2013).
19. L. Luo, I. Chatzakis, J. Wang, F. B. P. Niesler, M. Wegener, T. Koschny, and C. M. Soukoulis, "Broadband terahertz generation from metamaterials," Nat. Commun. **5**, 3055 (2014).
20. J. Gu, R. Singh, X. Liu, X. Zhang, Y. Ma, S. Zhang, S. A. Maier, Z. Tian, A. K. Azad, H. T. Chen, A. J. Taylor, J. Han, and W. Zhang, "Active control of electromagnetically induced transparency analogue in terahertz metamaterials," Nat. Commun. **3**, 1151 (2012).
21. D. R. Chowdhury, R. Singh, A. J. Taylor, H. T. Chen, and A. K. Azad, "Ultrafast manipulation of near field coupling between bright and dark modes in terahertz metamaterial," Appl. Phys. Lett. **102**, 011122 (2013).
22. F. Miyamaru, H. Morita, Y. Nishiyama, T. Nishida, T. Nakanishi, M. Kitano, and M. W. Takeda, "Ultrafast optical control of group delay of narrow-band terahertz waves," Sci. Rep. **4**, 4346 (2014).
23. S. H. Lee, M. Choi, T. T. Kim, S. Lee, M. Liu, X. Yin, H. K. Choi, S. S. Lee, C. G. Choi, S. Y. Choi, X. Zhang, and B. Min, "Switching terahertz waves with gate-controlled active graphene metamaterials," Nat. Mater. **11**, 936–941 (2012).
24. M. J. Dicken, K. Aydin, I. M. Pryce, L. A. Sweatlock, E. M. Boyd, S. Walavalkar, J. Ma, and H. A. Atwater, "Frequency tunable near-infrared metamaterials based on VO_2 phase transition," Opt. Express **17**, 18330–18339 (2009).
25. L. Kang, Q. Zhao, H. Zhao, and J. Zhou, "Magnetically tunable negative permeability metamaterial composed by split ring resonators and ferrite rods," Opt. Express **16**, 8825–8834 (2008).
26. J. Wang, S. Liu, S. Guruswamy, and A. Nahata, "Reconfigurable liquid metal based terahertz metamaterials via selective erasure and refilling to the unit cell level," Appl. Phys. Lett. **103**, 221116 (2013).
27. W. M. Zhu, A. Q. Liu, X. M. Zhang, D. P. Tsai, T. Bourouina, J. H. Teng, X. H. Zhang, H. C. Guo, H. Tanoto, T. Mei, G. Q. Lo, and D. L. Kwong, "Switchable magnetic metamaterials using micromachining processes," Adv. Mater. **23**, 1792–1796 (2011).

28. W. M. Zhu, A. Q. Liu, W. Zhang, J. F. Tao, T. Bourouina, J. H. Teng, X. H. Zhang, Q. Y. Wu, H. Tanoto, H. C. Guo, G. Q. Lo, and D. L. Kwong, "Polarization dependent state to polarization independent state change in THz metamaterials," Appl. Phys. Lett. **99**, 221102 (2011).
29. W. M. Zhu, A. Q. Liu, T. Bourouina, D. P. Tsai, J. H. Teng, X. H. Zhang, G. Q. Lo, D. L. Kwong, and N. I. Zheludev, "Microelectromechanical maltese-cross metamaterial with tunable terahertz anisotropy," Nat. Commun. **3**, 1274 (2012).
30. X. Li, T. Yang, W. Zhu, and X. Li, "Continuously tunable terahertz metamaterial employing a thermal actuator," Microsys. Technol. **19**, 1145–1151 (2013).
31. H. Tao, A. C. Strikwerda, K. Fan, W. J. Padilla, X. Zhang, and R. D. Averitt, "Reconfigurable terahertz metamaterials," Phys. Rev. Lett. **103**, 147401 (2009).
32. Y. S. Lin, Y. Qian, F. Ma, Z. Liu, P. Kropelnicki, and C. Lee, "Development of stress-induced curved actuators for a tunable THz filter based on double split-ring resonators," Appl. Phys. Lett. **102**, 111908 (2013).
33. F. Ma, Y. Qian, Y. S. Lin, H. Liu, X. H. Zhang, Z. Liu, J. M. L. Tsai, and C. Lee, "Polarization-sensitive microelectromechanical systems based tunable terahertz metamaterials using three dimensional electric split ring resonator arrays," Appl. Phys. Lett. **102**, 161912 (2013).
34. Y. S. Lin, F. Ma, and C. Lee, "Three-dimensional movable metamaterials using electric split ring resonators," Opt. Lett. **38**, 3126–3128 (2013).
35. F. Ma, Y. S. Lin, X. H. Zhang, and C. Lee, "Tunable multiband terahertz metamaterials using a reconfigurable electric split-ring resonator array," Light: Sci. Appl. **3**, e171 (2014).
36. Z. Han, K. Kohno, H. Fujita, K. Hirakawa, and H. Toshiyoshi, "MEMS reconfigurable metamaterial for terahertz switchable filter and modulator," Opt. Express **22**, 21326–21339 (2014).
37. Z. Han, K. Kohno, H. Fujita, K. Hirakawa, and H. Toshiyoshi, "Tunable terahertz filter and modulator based on electrostatic MEMS reconfigurable SRR array," IEEE J. Sel. Top. Quantum Electron. **21**, 1–9 (2015).
38. M. Unlu, M. R. Hashemi, C. W. Berry, S. Li, S.-H. Yang, and M. Jarrahi, "Switchable scattering meta-surfaces for broadband terahertz modulation," Sci. Rep. **4**, 5708 (2014).
39. M. Unlu and M. Jarrahi, "Miniature multi-contact MEMS switch for broadband terahertz modulation," Opt. Express **22**, 32245–32260 (2014).
40. C. P. Ho, P. Pitchappa, Y. S. Lin, C. Y. Huang, P. Kropelnicki, and C. Lee, "Electrothermally actuated microelectromechanical systems based omega-ring terahertz metamaterial with polarization dependent characteristics," Appl. Phys. Lett. **104**, 161104 (2014).
41. A. Lalas, N. Kantartzis, and T. Tsiboukis, "Tunable terahertz metamaterials by means of piezoelectric MEMS actuators," Europhys. Lett. **107**, 58004 (2014).
42. P. Pitchappa, C. P. Ho, L. Dhakar, Y. Qian, N. Singh, and C. Lee, "Periodic array of subwavelength MEMS cantilevers for dynamic manipulation of terahertz waves," J. Microelectromech. Syst. **24**, 525–527 (2015).
43. T. J. Cui, M. Q. Qi, X. Wan, L. Zhao, and Q. Cheng, "Coding metamaterials, digital metamaterials and programmable metamaterials," Light: Sci. Appl. **3**, e218 (2014).
44. B. Florijn, C. Coulais, and M. Hecke, "Programmable mechanical metamaterials," Phys. Rev. Lett. **113**, 175503 (2014).
45. A. Lalas, N. Kantartzis, and T. Tsiboukis, "Programmable terahertz metamaterials through V-beam electrothermal devices," Appl. Phys. A **117**, 433–438 (2014).
46. Y. Yuan, C. Bingham, T. Tyler, S. Palit, T. H. Hand, W. J. Padilla, D. R. Smith, N. M. Jokerst, and S. A. Cummer, "Dual-band planar electric metamaterial in the terahertz regime," Opt. Express **16**, 9746–9752 (2008).
47. J. Hendrickson, J. Guo, B. Zhang, W. Buchwald, and R. Soref, "Wideband perfect light absorber at midwave infrared using multiplexed metal structures," Opt. Lett. **37**, 371–373 (2012).
48. B. Zhang, J. Hendrickson, and J. Guo, "Multispectral near-perfect metamaterial absorbers using spatially multiplexed plasmon resonance metal square structures," J. Opt. Soc. Am. B **30**, 656–662 (2013).
49. N. Katsarakis, T. Koschny, M. Kafesaki, E. N. Economou, and C. M. Soukoulis, "Electric coupling to the magnetic resonance of split ring resonators," Appl. Phys. Lett. **84**, 2943–2945 (2004).
50. C. M. Soukoulis, T. Koschny, J. Zhou, M. Kafesaki, and E. N. Economou, "Magnetic response of split ring resonators at terahertz frequencies," Phys. Status Solidi B **244**, 1181–1187 (2007).
51. J. B. Pendry, A. J. Holden, D. J. Robbins, and W. J. Stewart, "Magnetism from conductors and enhanced nonlinear phenomena," IEEE Trans. Microwave Theory Technol. **47**, 2075–2084 (1999).
52. W. J. Padilla, M. T. Aronsson, C. Highstrete, M. Lee, A. J. Taylor, and R. D. Averitt, "Electrically resonant terahertz metamaterials: theoretical and experimental investigations," Phys. Rev. B **75**, 041102R (2007).
53. J. F. O'Hara, E. Smirnova, H. T. Chen, A. J. Taylor, R. D. Averitt, C. Highstrete, M. Lee, and W. J. Padilla, "Properties of planar electric metamaterials for novel terahertz applications," J. Nanoelectron. Optoelectron. **2**, 90–95 (2007).
54. C. M. Bingham, H. Tao, X. Liu, R. D. Averitt, X. Zhang, and W. J. Padilla, "Planar wallpaper group metamaterials for novel terahertz applications," Opt. Express **16**, 18565–18575 (2008).
55. W. M. Zhang, G. Meng, and D. Chen, "Stability, nonlinearity and reliability of electrostatically actuated MEMS devices," Sensors **7**, 760–796 (2007).
56. Y. Qian, L. Lou, M. L. J. Tsai, and C. Lee, "A dual-silicon-nanowires based U-shape nanoelectromechanical switch with low pull-in voltage," Appl. Phys. Lett. **100**, 113102 (2012).